

**Electronic Supplementary Information**

9 May, 2020

MS. ID: SC-EDG-04-2020-001931

**Focusing, sorting, and separating microplastics by serial  
faradaic ion concentration polarization**

Collin D. Davies and Richard M. Crooks

<b><u>Table of Contents</u></b>	<b><u>Page</u></b>
Figure ESI-1: Solution conductivity calibration curve	ESI-2
Electrophoretic mobility measurements	ESI-3
Numerical simulations	ESI-3
Figure ESI-2: Normalized conductivity with BPE1 "on"	ESI-8
Figure ESI-3: Tris concentration with BPE1 and BPE2 "on"	ESI-9
Simulated rate of convection	ESI-10
Movie ESI-1: Sorting by fICP	ESI-11
Movie ESI-2: Focusing and sorting by serial fICP	ESI-12
Movie ESI-3: Focusing, sorting, and separating by serial fICP	ESI-12
References	ESI-14

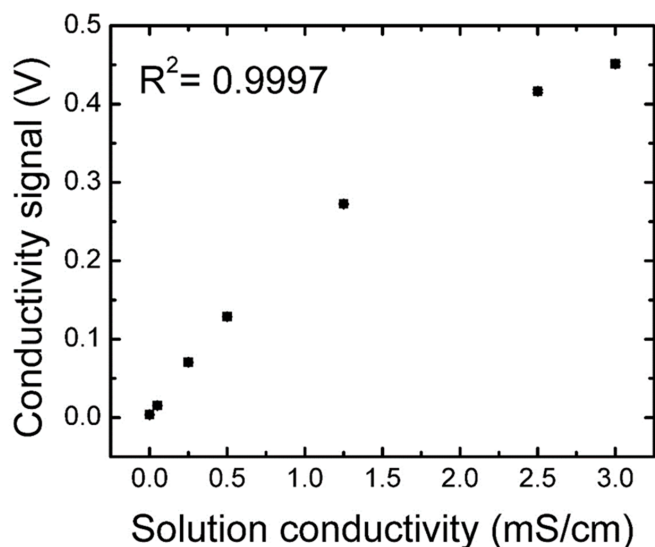


**Figure ESI-1. Solution conductivity calibration curve.**

Calibration curve used to correlate the measured conductivity signal (V) to solution conductivity (mS/cm). This is a representative calibration curve that was obtained using the conductivity microbands located in the top outlet channel (main text, Figure 3a). Similar calibration curves were obtained for the conductivity microbands located in the middle and bottom outlet channels. The calibration curves were generated as follows. First, solutions having the following conductivities were prepared from conductivity standard solutions: 0.05, 0.25, 0.50, 1.25, 2.50, and 3.00 mS/cm (NaCl conductivity standards, RICCA Chemical Company, Arlington, TX). Second, the solutions were flowed through the microfluidic channel by pressure-driven flow (PDF). Third, solution conductivity measurements were performed. Each data point represents the average of 100 measurements. The y error bars are smaller than the data points and thus are not apparent. The calibration curves deviate from linearity at high conductivities due to changes in the capacitance of the micron-scale Pt microbands.<sup>1</sup> Accordingly, the data were fit with second-order polynomial regressions. The average of the coefficients of determination ( $R^2$ ) for the calibration curves is  $0.9996 \pm 0.0003$  ( $n = 6$ ).

**Electrophoretic mobility measurements.** The electrophoretic mobilities of  $\mu\text{P1}$ ,  $\mu\text{P2}$ , and  $\mu\text{P3}$  were quantified by dynamic light scattering as follows. First, microplastic solutions were prepared by 100-fold dilution of the microplastic stock solutions in 10.0 mM Tris-HCl (pH 8.1). Second, the solutions were placed into a disposable folded capillary cell (Malvern Instruments, UK). Third, the cell was inserted into a Zetasizer Nano ZS (Malvern Instruments) and the electrophoretic mobility of the microplastics was measured. The reported electrophoretic mobility for each microplastic is the average of three measurements.

**Numerical simulations.** Finite element simulations were carried out using the COMSOL Multiphysics version 5.4 software package. Simulations were performed using a Dell Precision workstation (Model T7500) equipped with two Intel Xeon processors (2.40 GHz) and 108 GB of RAM. All simulations were performed at steady state.

Simulations were performed using a two-dimensional (2D) model based on the  $xy$ -plane of the microfluidic system shown in Figure 2a in the main text. The main channel was 200.0  $\mu\text{m}$  wide and each outlet channel was 66.7  $\mu\text{m}$  wide. The middle and top outlet channels were orientated at angles of 30° and 60°, respectively, from the bottom outlet channel. The bipolar electrode (BPE) poles were 50.0  $\mu\text{m}$  wide and located flush with the channel sidewalls. To capture the impact of serial faradaic ion concentration polarization (fICP) on the distribution of solution species within the channel, we modeled 250.0  $\mu\text{m}$  upstream of the leading edge of BPE1 and 250.0  $\mu\text{m}$  downstream of the trailing edge of BPE2. The length of BPE1 was 750.0  $\mu\text{m}$ , the length of BPE2 was 1000.0  $\mu\text{m}$ , and the gap between the BPEs was 710.0  $\mu\text{m}$ . Accordingly, the length of the channel modeled was

2960.0  $\mu\text{m}$  (250.0  $\mu\text{m}$  + 1000.0  $\mu\text{m}$  + 710.0  $\mu\text{m}$  + 750.0  $\mu\text{m}$  + 250.0  $\mu\text{m}$ ). The modeling domain is shown in Figure 4a in the main text.

Solution convection within the 2D model was simulated using the “Creeping Flow” interface in COMSOL Multiphysics. This interface solves the Navier-Stokes equation for incompressible flow of a viscous fluid (eqs ESI-1 and ESI-2).

$$\rho(u \cdot \nabla)u = \nabla \cdot [-pI + \mu(\nabla u + (\nabla u)^T)] + f_v \quad (\text{ESI-1})$$

$$\rho \nabla \times u = 0 \quad (\text{ESI-2})$$

Here,  $\rho$  is the density of the solution,  $u$  is the velocity vector of the solution,  $\mu$  is its dynamic viscosity,  $p$  is pressure,  $I$  is the identity matrix,  $T$  is temperature, and  $f_v$  is the volume force vector.

The right boundary of the model was taken to be the inlet and the left ends of the three secondary channels were taken to be the outlets. The inlet and outlets were modeled as pressure boundaries ( $p = 0$ ) and the channel sidewalls (remaining boundaries) were modeled as an electroosmotic velocity formulated according to the Helmholtz-Smoluchowski equation and calculated using the simulated local electric field. The zeta potential of the channel sidewalls was taken to be  $-50 \text{ mV}$ .<sup>2</sup>

Mass transport within the model was simulated with the “Nernst-Planck” interface. This interface solves the Nernst-Planck equation with the electroneutrality condition to simulate the flux of species by convection, diffusion, and electromigration (eqs ESI-3 - ESI-7).

$$\nabla \cdot J_i + u \cdot \nabla c_i = R_i \quad (\text{ESI-3})$$

$$\nabla \cdot i = F \sum_i z_i R_i \quad (\text{ESI-4})$$

$$\sum_i z_i c_i = 0 \quad (\text{ESI-5})$$

$$J_i = -D_i \nabla c_i - z_i \mu_{ep,i} F c_i \nabla \varphi \quad (\text{ESI-6})$$

$$i = F \sum_i z_i (-D_i \nabla c_i - z_i \mu_{ep,i} F c_i \nabla \varphi) \quad (\text{ESI-7})$$

Here,  $J_i$  is flux,  $c_i$  is concentration,  $R_i$  is the rate of reaction,  $z_i$  is the charge,  $D_i$  is the diffusion coefficient, and  $\mu_{ep,i}$  is the

electrophoretic mobility, all for species  $i$ .  $F$  is the Faraday.  $\varphi$  is the electric potential. The inlet was taken to have an inflow of 10.0 mM Tris-HCl buffer at pH 8.1. The concentrations of  $\text{TrisH}^+$ ,  $\text{Tris}$ , and  $\text{Cl}^-$  were determined from the pKa of Tris buffer at 20 °C (pKa = 8.24, calculated using the Debye-Hückel model).<sup>3,4</sup> The concentrations of  $\text{H}^+$  and  $\text{OH}^-$  were determined from the pH.

The inlet was taken to have a steady-state current density of 573.91 A/m<sup>2</sup> (1.32  $\mu\text{A}$  / (11.5  $\mu\text{m}$  · 200.0  $\mu\text{m}$ )) and the potential of the outlet boundaries was 0 V. The poles of BPE1 and BPE2 were taken to have current densities of 266.67 A/m<sup>2</sup> (0.60  $\mu\text{A}$  / (45.0  $\mu\text{m}$  · 50.0  $\mu\text{m}$ )) and 328.89 A/m<sup>2</sup> (0.74  $\mu\text{A}$  / (45.0  $\mu\text{m}$  · 50.0  $\mu\text{m}$ )), respectively. The value of the current densities at the cathodic poles of the BPEs was negative and the value of the current densities at the anodic poles of the BPEs was positive. The local current density across each BPE pole was assumed to be governed by a linear dependence on the axial position.<sup>5</sup> Specifically, the current density was 0 at the interior edge of each pole ( $x = 300, 1200, 2010, \text{ and } 2660 \mu\text{m}$ ) and had a maxima at the exterior edge of each pole ( $x = 250, 1250, 1960, \text{ and } 2710 \mu\text{m}$ ). Water electrolysis (eqs 1 and 3 in the main text) was modeled by fluxes at the poles of the BPEs and proceeded with 100% faradaic efficiency.<sup>2</sup> The production of  $\text{H}_2$  and  $\text{O}_2$  by water reduction and oxidation, respectively, was not accounted for in the model.

Following electrochemical water electrolysis, Tris buffer chemistry was simulated (eqs 2 and 4 in the main text).  $\text{TrisH}^+$  neutralization (i.e., Tris formation) was simulated using a reaction rate equation (eq ESI-8).

$$R_{\text{Tris}} = -(k_{f,\text{neut}}c_{\text{Tris}}) + (k_{b,\text{neut}}c_{\text{TrisH}^+}c_{\text{OH}^-}) + (k_{f,\text{neut}}c_{\text{TrisH}^+}) - (k_{b,\text{neut}}c_{\text{Tris}}c_{\text{H}^+}) \quad (\text{ESI-8})$$

Here,  $R_{Tris}$  is the rate of Tris formation. The previously reported reaction rate constants for Tris buffer neutralization were assumed to also describe Tris buffer reionization.<sup>2</sup> Accordingly,  $k_{f,neut}$  and  $k_{b,neut}$  are the forward and backward reaction rate constants, respectively, for both Tris buffer neutralization and reionization. Therefore,  $R_{Tris} = -R_{TrisH^+}$ .

The effect of Tris buffer chemistry on  $H^+$  was simulated using a second reaction rate equation (ESI-9).

$$R_{H^+} = (k_{f,hydro}c_{H_2O}) - (k_{b,hydro}c_{H^+}c_{OH^-}) + (k_{f,neut}c_{TrisH^+}) - (k_{b,neut}c_{Tris}c_{H^+}) \quad (ESI-9)$$

Here,  $R_{H^+}$  is the rate of  $H^+$  formation and  $k_{f,hydro}$  and  $k_{b,hydro}$  are the forward and backward reaction rate constants, respectively, for water self-ionization.<sup>2</sup> The concentration of water (55.5 M) was taken to be constant throughout the modeling domain.

The effect of Tris buffer chemistry on  $OH^-$  was simulated using a third reaction rate equation (ESI-10).

$$R_{OH^-} = (k_{f,hydro}c_{H_2O}) - (k_{b,hydro}c_{H^+}c_{OH^-}) + (k_{f,neut}c_{Tris}) - (k_{b,neut}c_{TrisH^+}c_{OH^-}) \quad (ESI-10)$$

Here,  $R_{OH^-}$  is the rate of  $OH^-$  formation.

Solution conductivity ( $\kappa$ ) was calculated from the simulated distribution of solution species using eq ESI-11.

$$\kappa = \sum_i c_i \mu_{ep,i} (z_i F)^2 \quad (ESI-11)$$

A user-controlled mesh was used to solve the multiphysics model. A relaxed mesh (maximum element size = 6.92  $\mu\text{m}$ , minimum element size = 0.0207  $\mu\text{m}$ ) optimized for fluid dynamics was used throughout the majority of the modeled domain, while a more dense mesh (maximum element size = 1.50  $\mu\text{m}$ , minimum element size = 0.0207  $\mu\text{m}$ ) was employed near the BPE poles to enable accurate modeling of water electrolysis and the rapid Tris buffer chemistry. The quality of the mesh was confirmed by a mesh refinement study.

A parametric sweep of the magnitude of the currents passed through the BPEs was used to solve the model. The model was solved iteratively from  $i_{\text{BPE1}} = i_{\text{BPE2}} = 0 \mu\text{A}$  to  $i_{\text{BPE1}} = 0.60 \mu\text{A}$  and  $i_{\text{BPE2}} = 0.74 \mu\text{A}$  using a current step of  $0.01 \mu\text{A}$ . The solution for each iteration was used to define the initial conditions for the next iteration.

Complete details for the parameters, geometry dimensions, and interface settings are available within the accompanying COMSOL Multiphysics report.

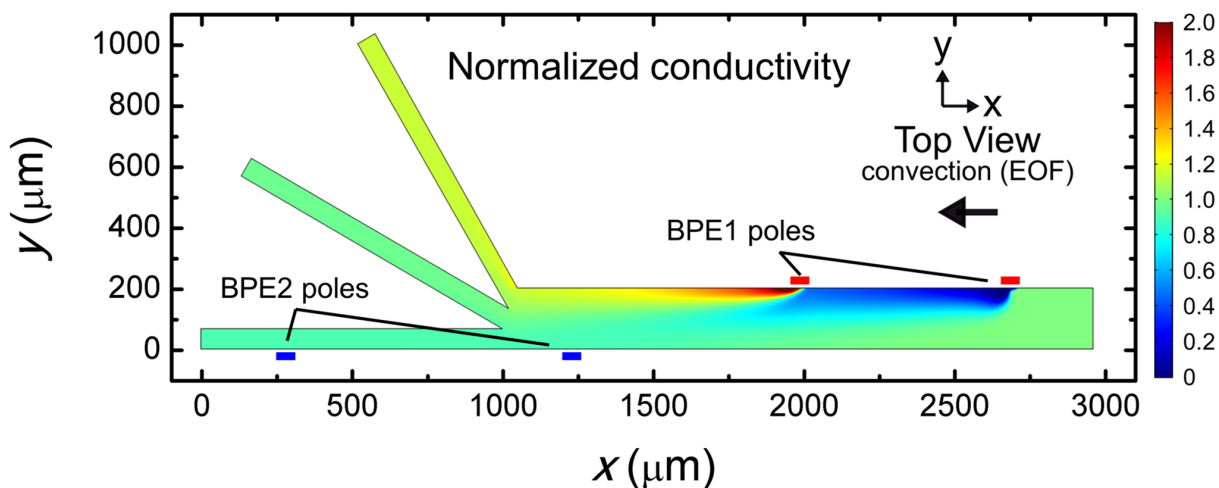


**Figure ESI-2. Normalized conductivity with BPE1 "on".** Steady-state simulation results for a solution containing 10.0 mM Tris buffer (pH 8.1), and with  $i_{\text{tot}} = 1.32 \mu\text{A}$  and  $i_{\text{BPE1}} = 0.60 \mu\text{A}$ . Plot of solution conductivity throughout the channel. Conductivity values are normalized to the conductivity of bulk solution. The range of the color scale bar is truncated for emphasis. The red and blue rectangles indicate the position of the poles of BPE1 and BPE2, respectively.

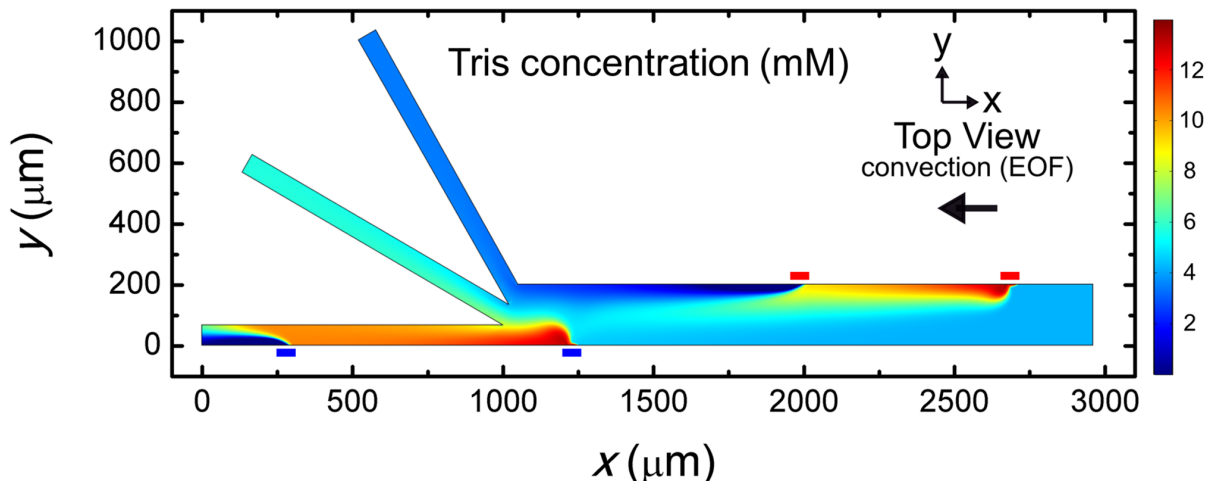


**Figure ESI-3. Tris concentration with BPE1 and BPE2 “on”.**

Steady-state simulation results for a solution containing 10.0 mM Tris buffer (pH 8.1), and with  $i_{\text{tot}} = 1.32 \mu\text{A}$ ,  $i_{\text{BPE1}} = 0.60 \mu\text{A}$ , and  $i_{\text{BPE2}} = 0.74 \mu\text{A}$ . Distribution of Tris along the channel length. The red and blue rectangles indicate the position of the poles of BPE1 and BPE2, respectively. The BPE poles in the 2D model are positioned flush with the channel sidewalls. Accordingly, the majority of  $\text{TrisH}^+$  neutralized near the cathodic pole of BPE2 does not diffuse beyond  $y = 67 \mu\text{m}$  and enter the middle outlet channel. Thus, most Tris formed near the cathodic pole of BPE2 flows downstream and enters the bottom outlet channel. Here, it is reionized by  $\text{H}^+$  generation at the anodic edge of BPE2.

**Simulated rate of convection.** The simulated result shown in Figure 4d in the main text is consistent with the following explanation. Connecting the microbands that comprise BPE1 with a jumper wire shunts ~46% of  $i_{\text{tot}}$  through BPE1 ( $i_{\text{BPE1}}$ ) and forms an ion depletion zone (IDZ) and ion enrichment zone (IEZ) in solution by fICP (shown most clearly in Figure 3b and Figure 4c in the main text). The resulting electric field gradient near the leading edge of the cathodic pole of BPE1 ( $x = 2710\text{--}2800 \mu\text{m}$ ) increases the local rate of convection by electroosmotic flow (EOF) and, because the solution is incompressible, creates a pressure gradient along the channel length. This produces a PDF from right to left, as shown by the parabolic flow profile at  $x = 2900 \mu\text{m}$ .

Shunting a large percentage of  $i_{\text{tot}}$  through BPE1 decreases the magnitude of the current passed in solution between the poles of BPE1.<sup>2,6</sup> Therefore, solution flow in this region of the channel ( $x = 2100\text{--}2500 \mu\text{m}$ ) is controlled by relatively weak EOF and pressure gradients. The current through BPE1 is converted to ionic current at the anodic pole of BPE1. The presence of an IEZ along the upper sidewall downstream of BPE1 (Figure 4c, main text) leads to a weak electric field in solution and a corresponding slow flow rate along the upper sidewall ( $x = 1500\text{--}1960 \mu\text{m}$ ). Therefore, the majority of solution continues downstream through a restricted region of the channel width ( $y = 30\text{--}150 \mu\text{m}$ ) at an elevated flow rate.

The explanation for the observed rates of convection near the cathodic pole of BPE2 ( $x = 1000\text{--}1250 \mu\text{m}$ ) is similar to that provided for convection near the cathodic pole of BPE1. However, in this case, the presence of the channel trifurcation increases the complexity of flow in this region. Although ~56% of  $i_{\text{tot}}$  passes through BPE2 ( $i_{\text{BPE2}}$ ), the majority of the remaining ~44% passes to the negative driving electrodes located in the

outlet reservoirs through the top and middle outlet channels. Because the magnitude of current is inversely proportional to solution resistance, the current density, and thus the rate of EOF, at the entrances to the top and middle outlet channels is largest along the upper sidewalls of each channel ( $y = 200 \mu\text{m}$  and  $133 \mu\text{m}$ , respectively). However, downstream from the entrances to the top and middle outlet channels, the conductivities of the solutions (see Figure 4c, main text), and thus the rates of EOF, are nearly uniform across the channel widths.

The rate of convection in the bottom outlet channel is influenced by the presence of BPE2. Specifically, shunting a large portion of  $i_{\text{tot}}$  through BPE2 decreases the magnitude of the current passed in solution between the poles of BPE2. Therefore, solution flow in this region of the bottom outlet channel ( $x = 300\text{--}1000 \mu\text{m}$ ) is controlled by relatively weak EOF and pressure gradients. However, the return of  $i_{\text{BPE2}}$  to solution at the anodic end of BPE2 results in an increase in the rate of convection downstream ( $x = 0\text{--}250 \mu\text{m}$ ), despite the presence of an IEZ in solution. This is due to the elevated current density in this portion of the microchannel.

**Movie ESI-1. Sorting by fICP.** Movie ESI-1 shows the manipulation of BODIPY<sup>2-</sup> and  $\mu\text{P1}$  during a fICP experiment using Tris buffer in a trifurcated channel. Movie ESI-1 was collected as follows. First, equal heights of solution containing  $1.0 \mu\text{M}$  BODIPY<sup>2-</sup>,  $1.5 \text{ pM}$   $\mu\text{P1}$ , and  $10.0 \text{ mM}$  Tris buffer (pH 8.1) were added to each reservoir resulting in zero PDF. Second, the video begins with solution moving right to left in the channel by EOF (driving voltage =  $25.0 \text{ V}$ ). Third, the microbands comprising the BPE (Scheme 2b, main text) were connected and fICP commenced. Finally, the BPE microbands were disconnected, fICP stopped, and the microplastic flow rate returned to its original value.

**Movie ESI-2. Focusing and sorting by serial fICP.** Movie ESI-2 shows the manipulation of BODIPY<sup>2-</sup> and  $\mu$ P1 during a serial fICP experiment using Tris buffer in a trifurcated channel. Movie ESI-2 was collected as follows. First, equal heights of solution containing 1.0  $\mu$ M BODIPY<sup>2-</sup>, 1.5 pM  $\mu$ P1, and 10.0 mM Tris buffer (pH 8.1) were added to each reservoir resulting in zero PDF. Second, the video begins with solution moving right to left in the channel by EOF (driving voltage = 25.0 V). Third, the microbands comprising BPE1 (Figure 2a, main text) were connected and fICP commenced. Fourth, the field of view moved upstream from the channel trifurcation to the anodic pole of BPE1, then to the cathodic pole of BPE1, and then back to the channel trifurcation. Fifth, the microbands comprising BPE2 (Figure 2a, main text) were connected and serial fICP commenced. Finally, the microbands comprising the two BPEs were disconnected, serial fICP stopped, and the microplastic flow rate returned to its original value.

**Movie ESI-3. Focusing, sorting, and separating by serial fICP.** Movie ESI-3 shows the manipulation of  $\mu$ P2 and  $\mu$ P3 during a serial fICP experiment using Tris buffer in a trifurcated channel. Movie ESI-3 was collected as follows. First, different heights of solution containing 150 fM  $\mu$ P2, 190 pM  $\mu$ P3, and 10.0 mM Tris buffer (pH 8.1) were added to the inlet and outlet reservoirs resulting in PDF from right to left ( $32 \pm 3$  nL/min,  $n = 7$ ). Second, the video begins with solution moving right to left in the channel by PDF. Third, the driving voltage (25.0 V) was applied across the channel length resulting in EOF from right to left. Fourth, the microbands comprising BPE2 (Figure 2a, main text) were connected and fICP commenced. Fifth, the microbands comprising BPE1 (Figure 2a, main text) were connected and serial fICP commenced. Sixth, the field of view moved upstream from the channel trifurcation to the

cathodic pole of BPE1, then to the anodic pole of BPE1, and then back to the channel trifurcation. Finally, the microbands comprising the two BPEs were disconnected, serial fICP stopped, and the microplastic flow rate returned to its original value.

## References

- 1 R. J. LeSuer, F.-R. F. Fan and A. J. Bard, *Anal. Chem.*, 2004, **76**, 6894–6901.
- 2 D. Hlushkou, R. K. Perdue, R. Dhopeswarkar, R. M. Crooks and U. Tallarek, *Lab Chip*, 2009, **9**, 1903–1913.
- 3 C. W. Davies, *J. Chem. Soc.*, 1938, 2093–2098.
- 4 R. N. Goldberg, N. Kishore and R. M. Lennen, *J. Phys. Chem. Ref. Data*, 2002, **31**, 231–370.
- 5 E. Sheridan, D. Hlushkou, R. K. Anand, D. R. Laws, U. Tallarek and R. M. Crooks, *Anal. Chem.*, 2011, **83**, 6746–6753.
- 6 R. K. Perdue, D. R. Laws, D. Hlushkou, U. Tallarek and R. M. Crooks, *Anal. Chem.*, 2009, **81**, 10149–10155.